metals

Article

Optimization Study on the Process Parameters for Molybdenum Milling

Xian Meng [1,*], Hao Xu [1], Haochen Li [2], Jinwen Cao [1], Jinyue Geng [1], Cong Yan [1], Xiang Cheng [2] and Heji Huang [1,3]

[1] State Key Laboratory of High Temperature Gas Dynamics, Institute of Mechanics, Chinese Academy of Sciences, Beijing 100190, China
[2] School of Mechanical Engineering, Shandong University of Technology, Zibo 255000, China
[3] School of Engineering Science, University of Chinese Academy of Sciences, Beijing 100049, China
* Correspondence: mengxian@imech.ac.cn

Abstract

Molybdenum (Mo), owing to its excellent properties, is widely used as a plasma-facing material and is recognized as a typical difficult-to-machine material. Achieving high-quality, low-damage machining is essential for ensuring the service reliability of Mo components. However, studies on the milling of Mo remain limited. Therefore, this study investigates a high-quality, low-damage milling technique for Mo based on analyses of milling force, machined surface roughness, and white layer formation. First, the effects of machining parameters, including radial depth of cut (a_e), spindle speed (n), and feed per tooth (f_z), on the responses, namely milling force (F) and surface roughness (R_a), were investigated. The relationships between milling force, surface roughness, and white layer formation were analyzed. Subsequently, the response surface methodology (RSM) was employed to reveal the influence mechanisms of the machining parameters and their interactions on the response variables. Finally, a Kriging surrogate model integrated with the Non-dominated Sorting Genetic Algorithm II (NSGA-II) was adopted to identify the optimal machining parameter combination for high-quality, low-damage milling. The results indicate that the milling force and white-layer thickness exhibit consistent increasing trends with increasing feed per tooth under the investigated conditions, demonstrating that controlling the milling force is an effective approach for achieving high-quality, low-damage milling of Mo. For the simultaneous minimization of milling force and surface roughness, the optimal machining parameters were determined to be a radial depth of cut of 0.2101 mm, a spindle speed of 10,090.7 rpm, and a feed per tooth of 0.01 mm/z. These findings provide valuable process parameter guidance for the precision machining of Mo components.

Keywords: milling; response surface methodology (RSM); surface integrity; multi-objective optimization

Check for updates

Academic Editor: Andrii Kostryzhev

Received: 20 July 2026
Revised: 17 August 2026
Accepted: 19 August 2026
Published: 21 August 2026

Copyright: © 2026 by the authors. Licensee MDPI, Basel, Switzerland. This article is an open access article distributed under the terms and conditions of the Creative Commons Attribution (CC BY) license.

1. Introduction

Molybdenum (Mo) exhibits a low sputtering yield and low hydrogen-isotope retention in plasma environments, making it an ideal candidate material for plasma-facing components (PFCs) and critical components in light-source chambers [1–3]. However, owing to its high strength, low ductility, and poor thermal conductivity, Mo is regarded as a typical difficult-to-machine material. During the machining of complex components, the machined surface is subjected to pronounced thermo-mechanical coupling, which promotes

the formation of a white layer and other surface defects. These machining-induced defects can facilitate fatigue crack initiation and delamination, thereby reducing the service reliability and lifetime of Mo components. Therefore, investigating the relationship between machining parameters and machined surface quality during the machining of Mo is of great significance.

Gokce et al. [4] conducted orthogonal milling experiments on Mo and reported that the feed speed had the greatest influence on the milling force, whereas the cutting speed exerted the most significant effect on surface roughness. Zhang et al. [5] investigated the formation mechanism of the white layer during the milling of nickel-based superalloy GH4169 and demonstrated that the white layer originated from grain refinement induced by dynamic recovery and recrystallization under thermo-mechanical coupling. Li et al. [6] found that the milling force and cutting temperature are the primary factors governing white layer formation. Specifically, the milling force induces severe plastic deformation in the machined surface, leading to grain refinement and promoting the formation of the white layer. Ekinovic et al. [7] optimized the milling parameters for hardened steel and identified the optimal ranges of cutting speed and feed speed, thereby mitigating the adverse effects of the white layer on the workpiece quality and surface integrity. Umbrello et al. [8] reported that the white layer primarily results from phase transformation induced by cutting heat, while plastic deformation caused by the milling force facilitates grain refinement and phase transformation. Tong et al. [9] investigated the milling of titanium alloy using ball-end mills with mesoscale geometric features and found that the microtextures reduced the tool-workpiece contact area, thereby decreasing the milling force and cutting temperature, which consequently reduced the white layer thickness. Mouralova et al. [10] conducted micro-milling experiments on pure Mo and investigated the surface morphology, burr height, and tool wear, with the optimized machining parameters determined through orthogonal experiments. Brown et al. [11] investigated the effects of cutting speed, tool wear, and up- and down-milling on white-layer formation and plastic deformation through orthogonal milling experiments and numerical simulations and found that severe plastic deformation, ploughing, and friction promote white-layer formation. Marçal et al. [12] performed high-resolution characterization of the machined white layer in Inconel 718 and revealed pronounced grain refinement within the white layer and evident lattice strain in the near-surface region. Hassanpour et al. [13] studied the relationship between cutting parameters and surface integrity during the minimum quantity lubrication (MQL) milling of AISI 4340 steel and demonstrated that cutting speed and feed speed are the key factors affecting white layer thickness. Xu et al. [14] optimized milling parameters by integrating response surface methodology (RSM) with the Non-dominated Sorting Genetic Algorithm II (NSGA-II), achieving the minimum milling force and surface roughness together with the maximum material removal rate. Qu [15], Lu [16], Zhou [17], Li [18], and others also employed NSGA-II to optimize milling process parameters.

This indicates that studies on the machining of Mo remain limited. Previous studies have shown that white layer formation is primarily governed by thermo-mechanical coupling during the cutting process [19]. Therefore, in this study, a flood cooling strategy was employed to suppress the influence of thermal effects on white layer formation, while the surface quality of milled Mo was improved through the optimization of milling process parameters. First, the effects of the machining parameters, including the radial depth of cut (a_e), spindle speed (n), and feed per tooth (f_z), on the response variables, namely the milling force (F) and surface roughness (R_a), were investigated, and the relationship between the response variables and white layer thickness was analyzed. Subsequently, response surface methodology (RSM) was employed to elucidate the effects of the machining parameters and their interactions on the response variables. Finally, the optimized machining param-

eters were determined by integrating a Kriging surrogate model with a multi-objective optimization algorithm.

2. Experimental Method and Material

2.1. Experimental Setup

The milling experiments were conducted on a CarverPMS23_A8 machining center with a maximum spindle speed of 36,000 rpm. The travel ranges of the X-, Y-, and Z-axes were 400 mm, 400 mm, and 230 mm, respectively. A 4 mm diameter cemented carbide end mill with four flutes, a helix angle of 35°, and a TiAlN coating was used in the experiments, and its specifications are listed in Table 1. The workpiece material was Mo with a purity of 99.95%, and the dimensions of the machined specimens were 20 mm × 30 mm × 60 mm. It was supplied by ATTL Advanced Materials Co., Ltd., Tianjin, China, and its relevant thermophysical properties are summarized in Table 2. The surface roughness, R_a, of the unmachined Mo specimens was measured at different locations, with an average value of 0.651 μm. During milling, an extreme-pressure emulsion was supplied by flood cooling at a concentration of 5% and a flow rate of 2.5 L/min. Three processing experiments were repeated under each condition. The experimental setup and measurement instruments are shown in Figure 1. R_a was measured perpendicular to the predominant milling lay, i.e., perpendicular to the feed direction. The cut-off wavelength was 0.8 mm, and the evaluation length was 4.0 mm (5 × 0.8 mm), with a Gaussian filter applied. Five measurements were performed at different locations on each machined surface, and their average was taken as the R_a value of each specimen. Three independent specimens were tested under each experimental condition. The reported values are the mean values of the three specimens, and the error bars represent the corresponding standard deviations. Milling force (F) was measured using a Kistler 9257B three-component dynamometer (Kistler Group, Winterthur, Switzerland). The cutting-force signals were acquired at a sampling frequency of 20 kHz. During the stable cutting stage, five different time intervals were selected. For each time interval, the instantaneous resultant milling force was first calculated at each sampling point as the square root of the sum of the squares of the three orthogonal force components (F_x, F_y, and F_z). The maximum resultant force within the interval was then taken as the representative milling force. The resultant forces obtained from the five intervals were then averaged and taken as the representative milling force for the corresponding experimental condition.

Table 1. Specifications of the milling cutter.

Materials	Diameter (mm)	Coating	Helix Angle (°)	Number of Flutes
Cemented carbide	4	TiAlN	35	4

Table 2. Thermophysical properties of Mo.

Property	Value
Coefficient of thermal expansion (ppm·K^{-1})	4.8
Yield strength (MPa)	600
Poisson's ratio	0.31
Vickers hardness (HV)	239
Elastic modulus (GPa)	329
Density (g·cm^{-3})	10.15
Specific heat capacity (J·kg^{-1}·K^{-1})	251

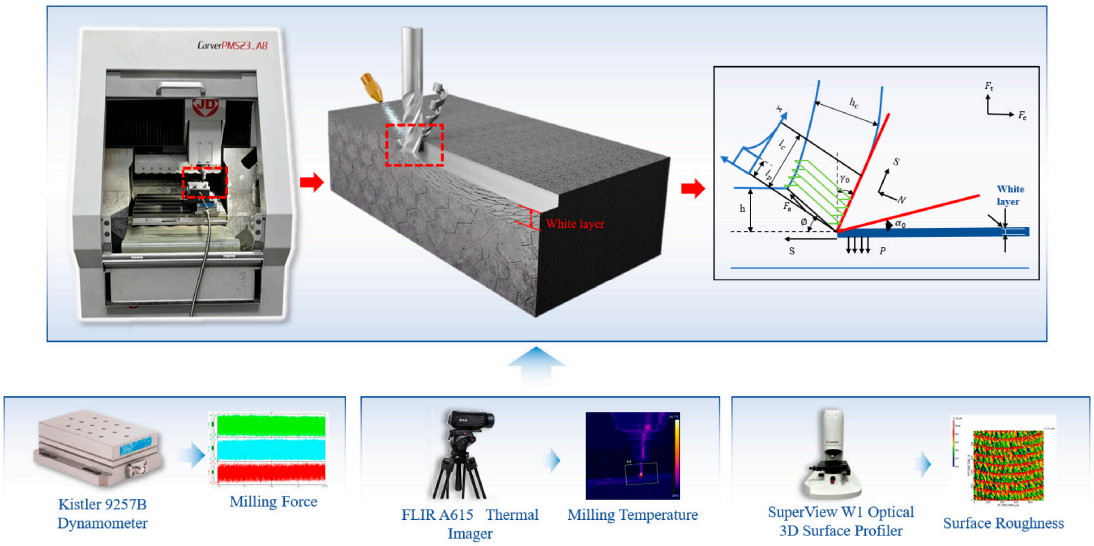


Figure 1. Experimental setup and measurement instruments.

2.2. Experimental Design

Based on previous milling studies of other difficult-to-machine materials, the milling force (F) and surface roughness (R_a) were selected as the response variables in this study, while the radial depth of cut (a_e), spindle speed (n), and feed per tooth (f_z) were chosen as the machining parameters. Milling experiments were conducted to investigate the effects of the machining parameters on the response variables. The milling parameters used in the experiments are listed in Table 3.

Table 3. Milling parameters used in the experiments.

Symbol	Control Factor	Level	Constant Level
1	Spindle speed n (rpm)	3000, 6000, 9000, 12,000, 15,000	a_p = 0.1 mm, f_z = 0.01 mm/z, a_e = 0.2 mm
2	Feed per tooth f_z (mm/z)	0.01, 0.02, 0.03, 0.04, 0.05	a_p = 0.1 mm, n = 12,000 rpm, a_e = 0.2 mm
3	Radial depth of cut a_e (mm)	0.2, 0.4, 0.6, 0.8, 1.0	a_p = 0.1 mm, n = 12,000 rpm, f_z = 0.01 mm/z

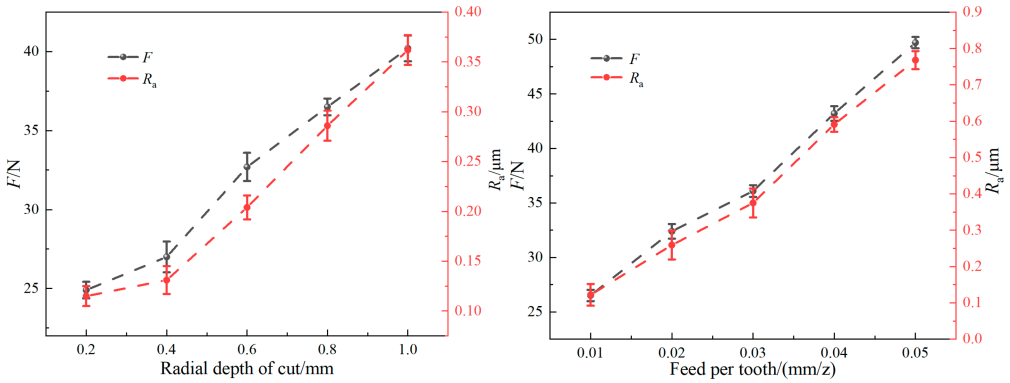
2.3. Results and Discussion

2.3.1. Effects of Machining Parameters on the Milling Force and Surface Roughness

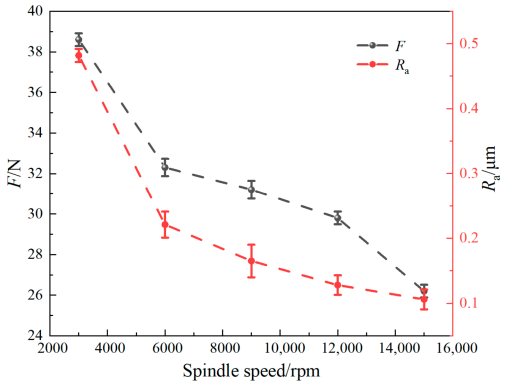
The effects of the machining parameters on the milling force (F) and surface roughness (R_a) are presented in Figure 2. As shown in Figure 2, increasing the feed per tooth (f_z) and radial depth of cut (a_e) leads to a larger undeformed chip thickness and a longer engaged cutting edge, thereby increasing the material removal rate and consequently the milling force. In contrast, the milling force decreases with the increase in spindle speed (n).

To assist in interpreting the decrease in milling force with increasing spindle speed, additional cutting-temperature measurements were performed under dry milling conditions while keeping the other machining parameters unchanged. Dry milling was adopted because the cutting fluid under flood cooling obscures the cutting region and interferes with the infrared radiation received by the thermal imager, making direct temperature measurement difficult. Therefore, the dry-milling temperature measurements were used only to identify the variation trend of cutting temperature with spindle speed and to assist

in explaining the corresponding variation in milling force. As shown in Figure 3, the cutting temperature increases with spindle speed. The resulting thermal softening of the workpiece material, accompanied by a reduction in the friction coefficient, contributes to the decrease in milling force. The underlying force-reduction mechanism was further analyzed using the dual-zone contact model [20–22], as expressed in Equations (1) and (2). As the spindle speed increases, both the milling speed and the strain rate in the primary shear zone increase, thereby intensifying the adiabatic shear effect and narrowing the shear band. This leads to an increase in the equivalent shear angle and, consequently, a reduction in the milling force [22]. In addition, higher milling speeds promote the periodic formation of continuous chips along the shear band, whereas fragmented chips associated with pronounced work hardening are more likely to form at lower speeds. The formation of continuous chips indicates a more stable cutting process with reduced force fluctuations, thereby contributing to lower surface roughness. It should be noted that the thermal environment under dry milling differs substantially from that under flood cooling. Therefore, the temperature results presented here are used only to interpret the variation in milling force and are not used to explain white-layer formation under flood-cooling conditions.



(**a**) F and R_a versus a_e. (**b**) F and R_a versus f_z.



(**c**) F and R_a versus n.

Figure 2. Effects of a_e, f_z, and n on the milling force (F) and surface roughness (R_a).

The variation in surface roughness (R_a) exhibits a trend similar to that of the milling force (F). As the feed per tooth (f_z) and radial depth of cut (a_e) increase, the milling force increases, which may induce machining vibrations. Meanwhile, the plastic deformation zone expands, leading to an increase in the residual surface profile height and, consequently, a higher surface roughness (R_a). In contrast, as the spindle speed (n) increases, the milling force decreases, and the residual surface profile height is reduced, resulting in a lower surface roughness (R_a).

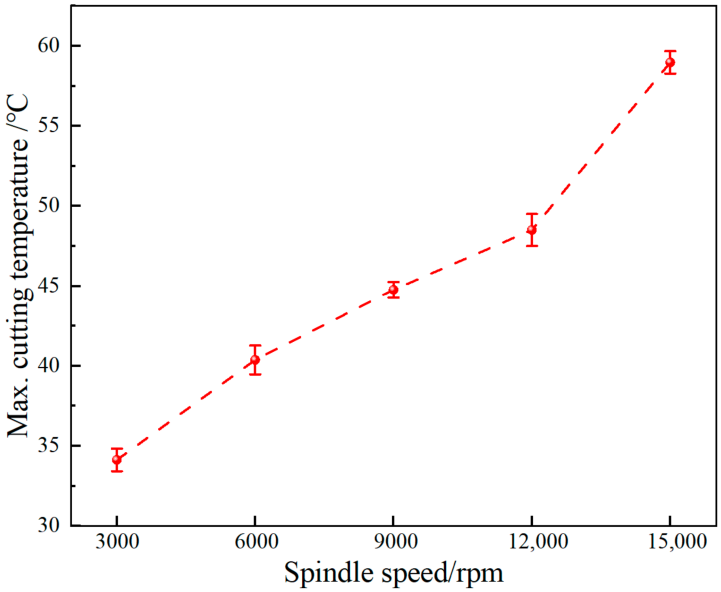


Figure 3. Effect of spindle speed (n) on the maximum cutting temperature (T_{max}).

$$\phi = \frac{\pi}{4} + \gamma_0 - \beta \tag{1}$$

$$F_c = \frac{\tau_s bh \cos(\beta - \gamma_0)}{\sin\phi \cos(\phi + \beta - \gamma_0)} \tag{2}$$

2.3.2. Effects of Machining Parameters on the White Layer

Previous studies have demonstrated that the white layer is formed through the combined effects of cutting heat and plastic deformation, exhibiting a pronounced thermo-mechanical coupling characteristic during its formation [19]. In the present study, flood cooling was employed to significantly reduce the temperature in the milling zone, thereby suppressing the influence of thermal effects on white layer formation to a certain extent. The single-factor experimental results indicate that the milling force (F) and surface roughness (R_a) exhibit similar variation trends. Since the feed per tooth (f_z) produces the largest variation in the milling force, the white layer thicknesses of the five specimens in Group B of Table 3 are further characterized and analyzed. Here, the criterion used to determine the white layer thickness was the maximum value measured from three cross-sections rather than the average value. Considering that the white layer is a form of machining-induced damage that may adversely affect component service performance, particularly fatigue life, the locally thickened regions are of particular concern. Because the white layer is non-uniformly distributed along the machined surface, the use of an average thickness may underestimate severe localized damage. Therefore, the maximum white layer thickness was selected as the evaluation index in this study.

The specimens were mounted in edge-retention resin and then mechanically ground and polished. The machined cross-sections were subsequently metallographically etched using Murakami's reagent [23]. After etching, a distinct microstructural difference between the machined surface layer and the substrate was observed, as shown in Figure 4. The variation in white layer thickness at different feed per tooth values (f_z) is presented in Figure 5. As f_z increases, both the milling force (F) and white layer thickness increase. This indicates that a higher milling force intensifies the tool-workpiece interaction and subjects the workpiece surface layer to stronger compressive and shear deformation, thereby aggravating plastic deformation and promoting white layer formation. Therefore, reducing F and R_a through the optimization of machining parameters helps mitigate machined surface damage and reduce the white layer thickness.

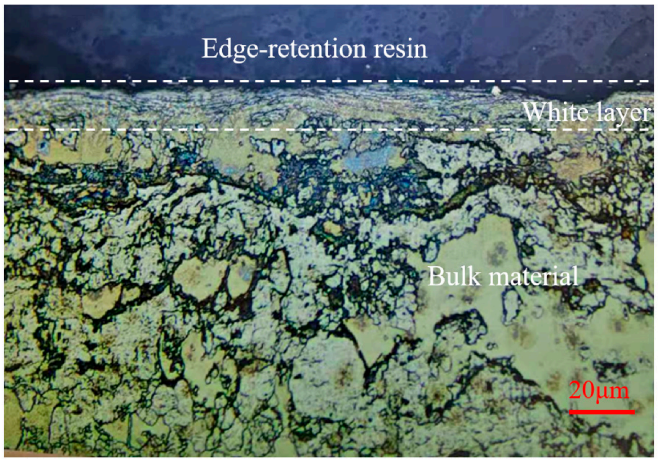


Figure 4. Metallographic morphology of the white layer.

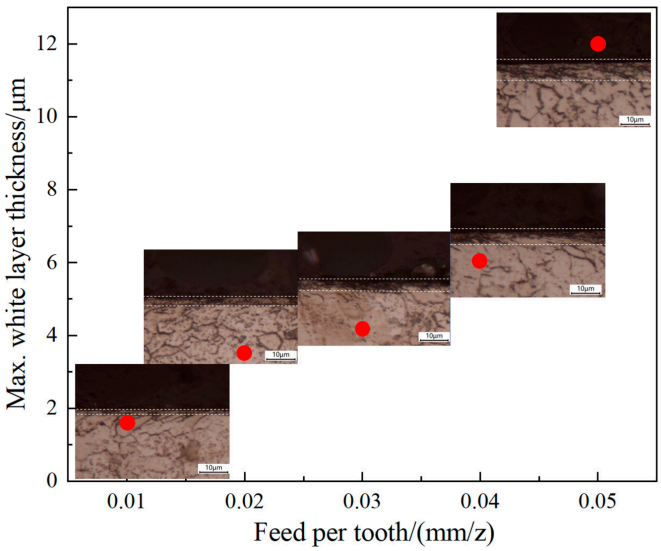
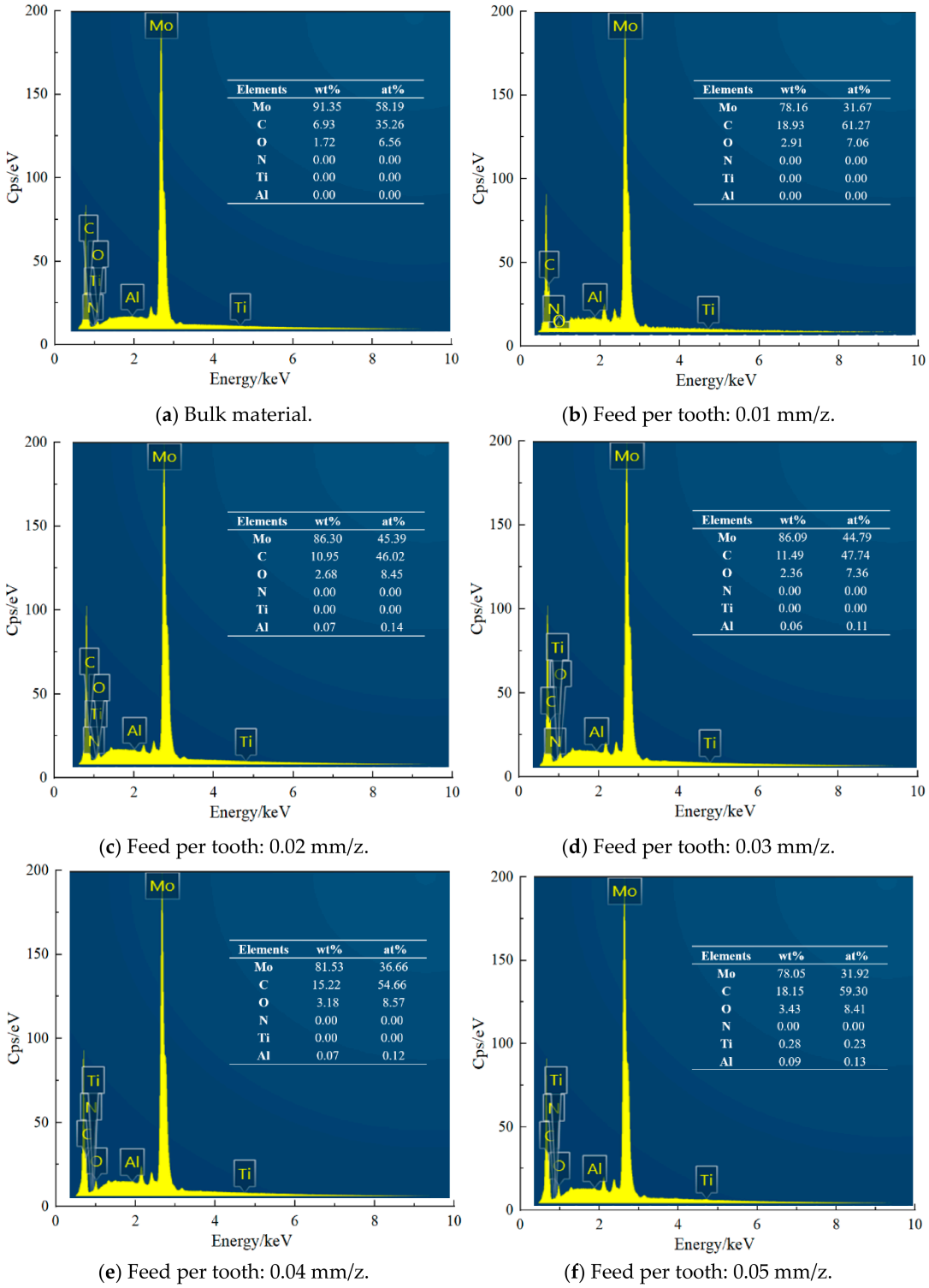


Figure 5. Effect of feed per tooth (f_z) on the maximum white layer thickness. The dashed lines indicate the boundaries of the white layer used for determining the maximum white-layer thickness.

After removing the edge-retention resin, the surface opposite the etched cross-section was selected for EDS analysis. Before measurement, this surface was mechanically ground and polished, followed by ultrasonic cleaning in absolute ethanol to minimize interference from residual resin, etchant residues, and the surface oxide layer. EDS line scans were performed across the Mo substrate and the white layers produced under different machining parameters to characterize variations in elemental distribution among the different regions. The EDS results are presented in Figure 6. The results show that Mo is the predominant element in both the substrate and the white layers formed under different machining conditions, with no evident overall change in chemical composition. This indicates that the white layer is primarily formed through microstructural evolution of the Mo substrate. Compared with the substrate, the white layer exhibits increased C and O contents. The increase in O content is likely associated with oxidation of the Mo surface during machining [24]. As the feed per tooth (f_z) increases, small amounts of Ti and Al are detected in the white-layer region, which may be related to increased wear of the TiAlN coating and subsequent material transfer caused by stronger tool–workpiece interaction.



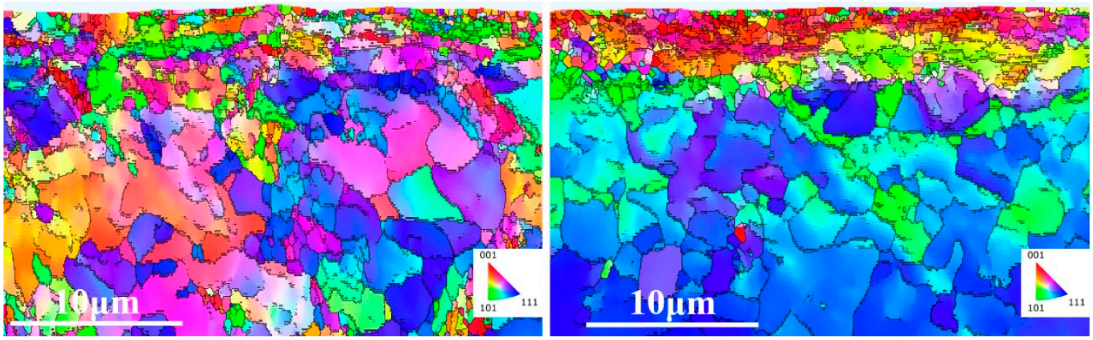
(**a**) Bulk material. (**b**) Feed per tooth: 0.01 mm/z.

(**c**) Feed per tooth: 0.02 mm/z. (**d**) Feed per tooth: 0.03 mm/z.

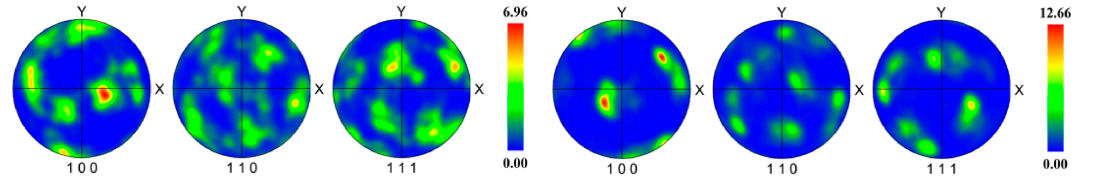
(**e**) Feed per tooth: 0.04 mm/z. (**f**) Feed per tooth: 0.05 mm/z.

Figure 6. EDS of the substrate and white layers under different feed per tooth values.

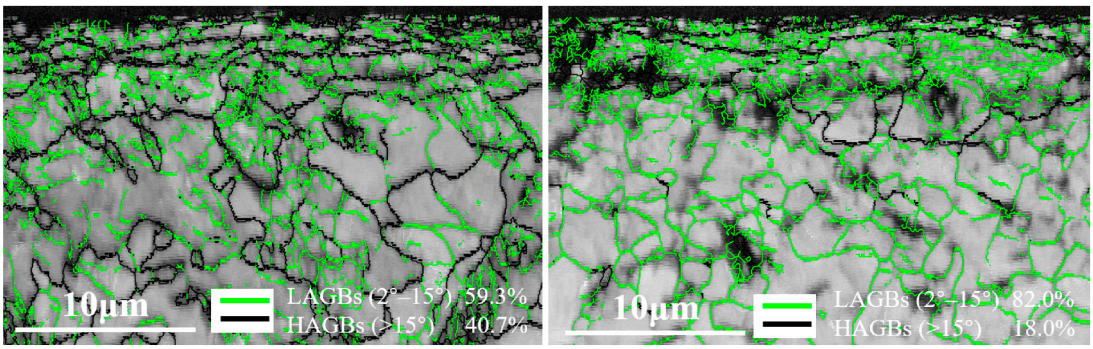
To further investigate the effect of the feed per tooth (f_z) on the white layer microstructure, two representative specimens, denoted as A and B, corresponding to $f_z = 0.05$ mm/z and $f_z = 0.02$ mm/z, respectively, were selected for EBSD analysis. The results are presented in Figure 7. Considering that the white layer thickness varies along the machined surface and the interface between the white layer and the substrate is irregular, the region within 5 μm beneath the machined surface was defined as the white layer for statistical analysis, while the region below this depth was regarded as the substrate.



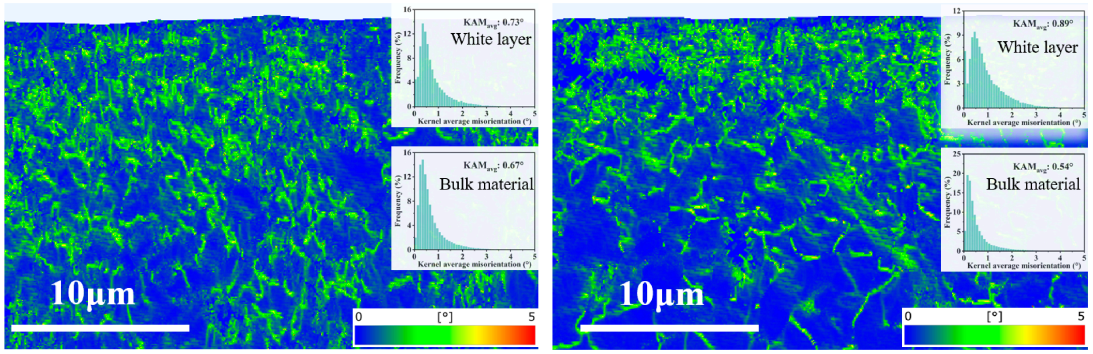
(**a**) IPF map of Sample A. (**b**) IPF map of Sample B.



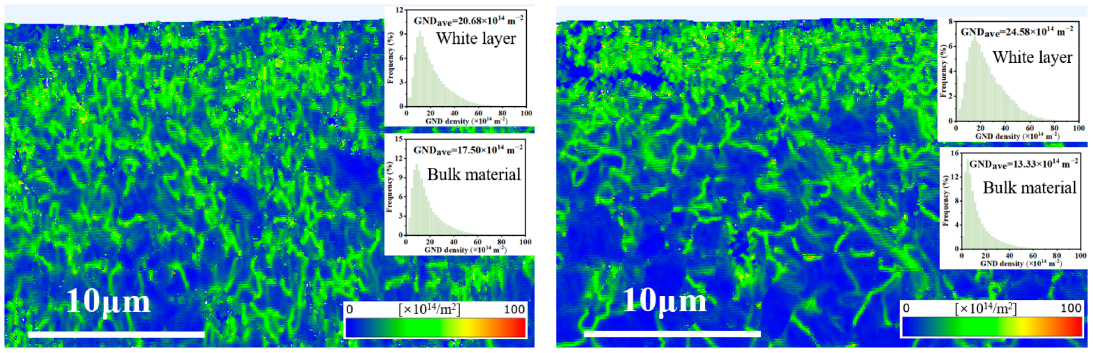
(**c**) PFs map of Sample A. (**d**) PFs map of Sample B.



(**e**) Grain boundary map of Sample A. (**f**) Grain boundary map of Sample B.



(**g**) KAM map of Sample A. (**h**) KAM map of Sample B.



(**i**) GND density map of Sample A. (**j**) GND density map of Sample B.

Figure 7. EBSD characterization results of specimens A and B.

The EBSD results indicate that both the white layer and the substrate of specimens A and B exhibit a pronounced {111}//ND preferred orientation, suggesting that the white layer retains part of the crystallographic orientation inherited from the substrate despite significant grain refinement. It shows that the average grain sizes of the white layer and substrate are 0.64 μm and 1.35 μm, respectively, for specimen A, and 0.60 μm and 1.78 μm, respectively, for specimen B. These results indicate that the compressive and shear actions exerted by the cutting tool during milling promote grain refinement in the surface layer. Although specimen A exhibits a thicker white layer than specimen B, their average grain sizes are comparable, indicating that the white layer thickness is not linearly correlated with the degree of grain refinement.

It further reveals that the maximum pole densities of specimens A and B are 6.96 and 12.66, respectively, from the pole figure analysis. The pole distribution of specimen A is relatively more dispersed, indicating a lower degree of crystallographic texture concentration. The grain boundary misorientation analysis shows that the fractions of low-angle grain boundaries (LAGBs) are 59.3% and 82.0% for specimens A and B, respectively. Moreover, the average kernel average misorientation (KAM) and geometrically necessary dislocation (GND) density in the white layer are 0.73° and 20.68 × 10^{14} m^{-2} for specimen A, and 0.89° and 24.58 × 10^{14} m^{-2} for specimen B, respectively. To evaluate the influence of the selected statistical depth, an additional sensitivity analysis was performed using 3 and 5 μm statistical regions for both specimens and an 8 μm region for specimen A. Although the absolute KAM and GND values varied slightly with the statistical depth, the relative trends between specimens A and B remained unchanged, indicating that the use of the fixed 5 μm statistical region does not affect the main conclusions of the EBSD analysis. The white layer formed under the lower feed per tooth exhibits more pronounced local lattice misorientation gradients and dislocation accumulation [25].

3. Response Surface Analysis

3.1. Response Surface Methodology

A Box–Behnken Design (BBD) based on response surface methodology (RSM) was employed to design the experiments and evaluate the effects of the machining parameters on the response variables. Each machining parameter was investigated at three levels. Based on the results of the single-factor experiments, a combination of low radial depth of cut (a_e), high spindle speed (n), and low feed per tooth (f_z) is favorable for achieving high-quality machining. Accordingly, the factors and levels adopted in the BBD are listed in Table 4.

Table 4. Factors and levels used in the BBD.

Level	Spindle Speed, n (rpm)	Feed per Tooth, f_z (mm/z)	Radial Depth of Cut, a_e (mm)
−1	6000	0.01	0.2
0	9000	0.02	0.4
1	12,000	0.03	0.6

The response surface experimental results are summarized in Table 5. Analysis of variance (ANOVA) and response surface plots are employed to investigate the relationships between the input variables, namely the radial depth of cut (a_e), spindle speed (n), and feed per tooth (f_z), and the response variables, namely the milling force (F) and surface roughness (R_a). Based on the RSM analysis, the complete second-order polynomial regression models for milling force (F) and surface roughness (R_a) were obtained as follows:

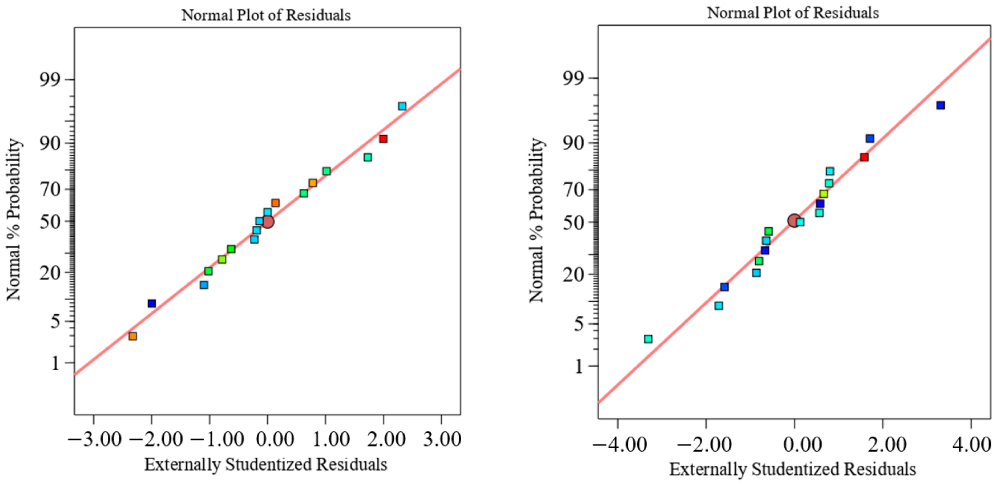
$$F = 223.1525 - 0.028097n - 5455.7075f_z - 32.81413a_e + 0.210742nf_z - 0.003347na_e + 2009.5f_za_e + 1.17353 \times 10^{-6}n^2 + 93195.5f_z^2 + 70.66375a_e^2 \quad (3)$$

$$R_a = 0.18975 + 0.000047n - 34.1125f_z - 0.2825a_e + 0.001408nf_z - 0.000068na_e + 52.00f_za_e - 2.20833 \times 10^{-9}n^2 + 376.25f_z^2 + 0.296875a_e^2 \quad (4)$$

Table 5. BBD experimental runs and corresponding responses.

	Input Variables			Response Variables	
Number	***n* (rpm)**	**f_z (mm/z)**	**a_e (mm)**	***F* (N)**	**R_a (μm)**
1	12,000	0.03	0.4	55.995	0.506
2	6000	0.02	0.6	65.187	0.336
3	9000	0.02	0.4	30.563	0.288
4	12,000	0.02	0.6	40.528	0.286
5	9000	0.02	0.4	32.942	0.240
6	9000	0.02	0.4	33.068	0.269
7	9000	0.03	0.2	43.119	0.253
8	9000	0.02	0.4	33.641	0.282
9	12,000	0.01	0.4	22.519	0.132
10	6000	0.01	0.4	63.691	0.144
11	9000	0.01	0.2	33.085	0.174
12	9000	0.01	0.6	40.414	0.168
13	6000	0.02	0.2	49.511	0.147
14	12,000	0.02	0.2	32.885	0.259
15	9000	0.02	0.4	37.983	0.246
16	9000	0.03	0.6	66.524	0.663
17	6000	0.03	0.4	71.878	0.349

Figure 8 presents the normal probability plots of the residuals for the milling force (F) and surface roughness (R_a), which are used to evaluate the deviations between the experimental and predicted values. The residuals are uniformly distributed around the reference line without any significant deviation, indicating that the residuals approximately follow a normal distribution. The coefficients of determination (R^2) of the models for F and R_a are 0.9802 and 0.9756, respectively, demonstrating that the developed models possess high prediction accuracy.



(**a**) Normal probability plot of residuals for F. (**b**) Normal probability plot of residuals for R_a.

Figure 8. Normal probability plots of residuals for the milling force (F) and surface roughness (R_a). The square symbols represent the residuals of the experimental data, and the solid line represents the theoretical normal-distribution reference line.

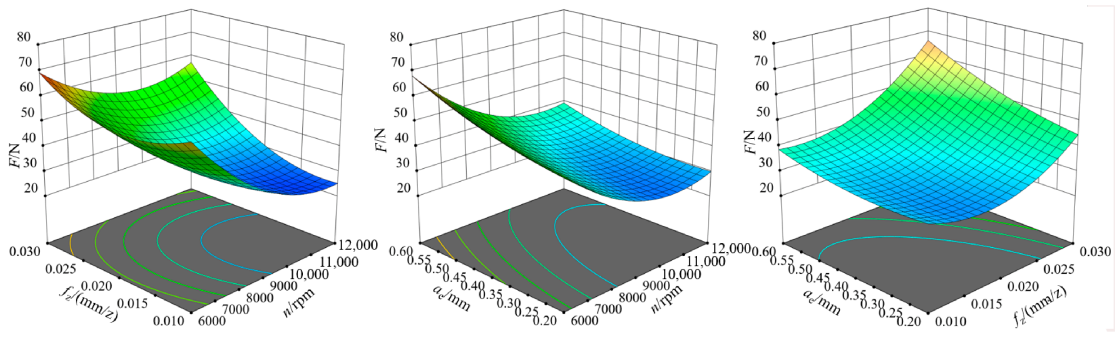
3.2. Response Analysis of the Milling Force

The significance of the developed model was evaluated by analysis of variance (ANOVA), and the corresponding results for the milling force are presented in Table 6. For ANOVA, the F-value reflects the significance of each term, whereas the *p*-value indicates the corresponding confidence level. A *p*-value less than 0.05 indicates that the corresponding term is statistically significant. The developed model exhibits a *p*-value below 0.0001, demonstrating that the regression model is highly significant. The lack-of-fit term has a *p*-value of 0.2693, indicating that the lack of fit is not statistically significant and that the residual variation is primarily attributed to random experimental error rather than other unaccounted factors. The significance analysis further reveals that all three machining parameters significantly affect the milling force. The influence of the machining parameters on the milling force decreases in the following order: spindle speed (n) > feed per tooth (f_z) > radial depth of cut (a_e).

Table 6. ANOVA results for the milling force model.

Source	Sum of Squares	df	Mean Square	F-Value	*p*-Value	
Model	3518.34	9	390.93	38.59	<0.0001	significant
A (n)	1208.84	1	1208.84	119.33	<0.0001	significant
B (f_z)	756.74	1	756.74	74.70	<0.0001	significant
C (a_e)	365.22	1	365.22	36.05	0.0005	significant
AB	159.88	1	159.88	15.78	0.0054	significant
AC	16.13	1	16.13	1.59	0.2474	
BC	64.61	1	64.61	6.38	0.0395	significant
A^2	469.69	1	469.69	46.37	0.0003	significant
B^2	365.70	1	365.70	36.10	0.0005	significant
C^2	33.64	1	33.64	3.32	0.1112	
Residual	70.91	7	10.13			
Lack of Fit	41.77	3	13.92	1.91	0.2693	not significant
Pure Error	29.14	4	7.29			
Cor Total	3589.25	16				

As shown in Figure 9, within the investigated parameter ranges, the milling force (F) decreases with increasing spindle speed (n) and increases with increasing radial depth of cut (a_e) and feed per tooth (f_z), which is consistent with the results of the single-factor experiments. The response surface further shows that the milling force reaches its maximum in the regions of low spindle speed and high feed per tooth. Therefore, while maintaining machining quality and productivity, the milling force can be effectively reduced by appropriately decreasing a_e and f_z and increasing n, thereby improving the stability of the machining process.



(**a**) Effects of n and f_z on F. (**b**) Effects of n and a_e on F. (**c**) Effects of f_z and a_e on F.

Figure 9. Three-dimensional response surfaces of the milling force (F) as a function of a_e, f_z, and n.

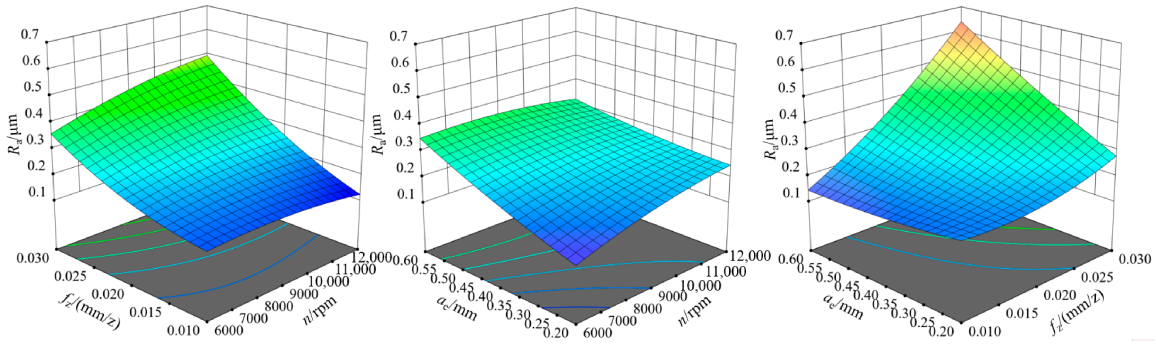
3.3. Response Analysis of Surface Roughness

The significance of the developed model was evaluated by analysis of variance (ANOVA), and the corresponding results for surface roughness (R_a) are presented in Table 7. The model has a p-value below 0.0001, indicating that it is highly significant. The lack-of-fit term has a p-value of 0.1120, indicating that the lack of fit is not statistically significant and that the residual variation is relatively small. The significance analysis shows that the feed per tooth (f_z) and radial depth of cut (a_e) significantly affect R_a. The influence of the machining parameters on R_a decreases in the following order: feed per tooth (f_z) > radial depth of cut (a_e) > spindle speed (n).

Table 7. ANOVA results for the surface roughness model.

Source	Sum of Squares	df	Mean Square	F-Value	*p*-Value	
Model	0.2846	9	0.0316	31.16	<0.0001	significant
A (n)	0.0054	1	0.0054	5.28	0.0552	
B (f_z)	0.1662	1	0.1662	163.78	<0.0001	significant
C (a_e)	0.0480	1	0.0480	47.36	0.0002	significant
AB	0.0071	1	0.0071	7.04	0.0328	significant
AC	0.0066	1	0.0066	6.47	0.0385	significant
BC	0.0433	1	0.0433	42.64	0.0003	significant
A^2	0.0017	1	0.0017	1.64	0.2412	
B^2	0.0060	1	0.0060	5.87	0.0458	significant
C^2	0.0006	1	0.0006	0.5852	0.4693	
Residual	0.0071	7	0.0010			
Lack of Fit	0.0053	3	0.0018	3.87	0.1120	not significant
Pure Error	0.0018	4	0.0005			
Cor Total	0.2917	16				

As shown in Figure 10, within the selected parameter ranges, surface roughness (R_a) increases with increasing radial depth of cut (a_e) and feed per tooth (f_z), whereas the effect of spindle speed (n) on R_a is relatively weak. The interaction between a_e and f_z has a pronounced influence on R_a. When both parameters increase simultaneously, the compressive action of the cutting tool and the plastic deformation of the machined surface are intensified, which is detrimental to achieving high surface quality.



(**a**) Effects of n and f_z on R_a (**b**) Effects of n and a_e on R_a (**c**) Effects of f_z and a_e on R_a

Figure 10. Three-dimensional response surfaces of surface roughness (R_a) as a function of a_e, f_z, and n.

4. Multi-Objective Optimization Analysis

The milling parameters were optimized by simultaneously minimizing the milling force (F) and surface roughness (R_a). The optimization in this study is specifically limited to identifying the parameter combination that minimizes these two responses within the

investigated parameter ranges. Since response surface-based multi-objective optimization is susceptible to the effects of empirical prediction models and subjective weight assignment, the Non-dominated Sorting Genetic Algorithm II (NSGA-II) was employed. NSGA-II is a classical multi-objective genetic algorithm that obtains a set of Pareto-optimal solutions through non-dominated sorting and a crowding-distance mechanism without requiring predefined objective weights [14–18].

In this study, 72 parameter combinations were generated using Latin hypercube sampling, and the corresponding F and R_a values were obtained through actual milling experiments. To ensure reproducibility of the data partitioning, a fixed random seed, rng (48), was used. The 72 experimental datasets were randomly divided using the holdout method into 50 training samples and 22 independent test samples. The test set, accounting for approximately 30% of the total data, was completely excluded from model-structure selection, hyperparameter determination, and cross-validation and was used only for the final evaluation of model generalization performance. Separate Kriging surrogate models were established for F and R_a using spindle speed n, radial depth of cut a_e, and feed per tooth f_z as the input variables. A Kriging model consists of a regression function describing the global trend of the response and a correlation function characterizing the correlation among the sample points. Three regression functions, regpoly0, regpoly1, and regpoly2, and five correlation functions, Gaussian, Spherical, Spline, Cubic, and Linear, were considered, resulting in 15 candidate model structures for each response. All candidate models were evaluated using only the 50 training samples. A repeated 10-fold cross-validation procedure with three independent repetitions was adopted. In each fold, 45 samples were used for model training, and the remaining 5 samples were used for validation, resulting in 30 validation runs for each candidate model. The mean absolute error (MAE) and root mean square error (RMSE) were used as the evaluation criteria. Only the input variables n, a_e, and f_z were normalized to [0, 1], whereas the response variables F and R_a were retained in their original physical units without normalization or scaling. Accordingly, all reported cross-validation MAE and RMSE values were calculated directly from the predicted and measured responses in their original units, i.e., N for F and μm for R_a. For the correlation-function hyperparameters θ, the initial value was set to [1, 1, 1], with each component constrained within the range of 10^{-3}–100. The hyperparameters were optimized by maximum likelihood estimation (MLE) and were re-estimated independently within each training fold. The repeated cross-validation results showed that the regpoly2 + Gaussian combination provided the best overall performance for F, with the lowest MAE of 0.010690 N and an RMSE of 0.0172 N, which was close to the minimum RMSE of 0.0168 N among all candidate models. For R_a, the regpoly2 + Linear combination achieved both the lowest MAE of 2.64×10^{-5} μm and the lowest RMSE of 3.06×10^{-5} μm. Therefore, regpoly2 + Gaussian and regpoly2 + Linear were selected as the final model structures for F and R_a, respectively. After model selection, the hyperparameters were re-estimated using all 50 training samples, and the final Kriging models were evaluated using the 22 independent test samples. The independent test set was not involved in model selection or hyperparameter optimization, while the model structures were selected exclusively through repeated cross-validation on the training set, thereby reducing the risk of overfitting.

It should be noted that the RSM and Kriging models were developed for different purposes and based on different experimental datasets. The RSM models were established using 17 BBD experiments, including five repeated center points, primarily to analyze the effects of the machining parameters and their interactions on F and R_a. The corresponding R^2 values for F and R_a were 0.9802 and 0.9756, respectively, indicating good fitting performance for the BBD data. In contrast, the Kriging models were established using the 72 Latin-hypercube experimental datasets to provide a broader experimental basis for the subsequent multi-objective

optimization. Because the two approaches were based on different experimental designs and datasets, their prediction errors were not directly compared.

The final Kriging surrogate models were subsequently used as objective functions in NSGA-II to obtain the Pareto-optimal solution set. Finally, the entropy-weight TOPSIS method was applied to determine objective weights according to the dispersion of the Pareto solutions and rank the candidate solutions, thereby identifying the optimal machining parameter combination for simultaneously minimizing F and R_a within the investigated parameter ranges. The optimization procedure is illustrated in Figure 11, the sampled data are listed in Table 8, and the corresponding mathematical models are expressed in Equations (5) and (6).

$$\min\{f_1(x) = \hat{F}(a_e, n, f_z), f_2(x) = \hat{R_a}(a_e, n, f_z)\} \tag{5}$$

$$\begin{cases} a_{emin} \le a_e \le a_{emax} \\ n_{min} \le n \le n_{max} \\ f_{zmin} \le f_z \le f_{zmax} \end{cases} \tag{6}$$

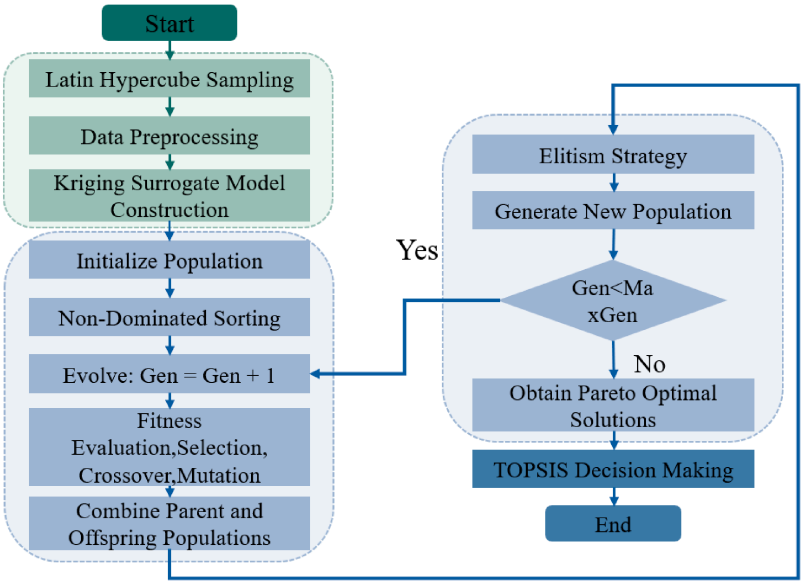


Figure 11. Flowchart of the multi-objective optimization procedure.

Table 8. Latin hypercube sampling data.

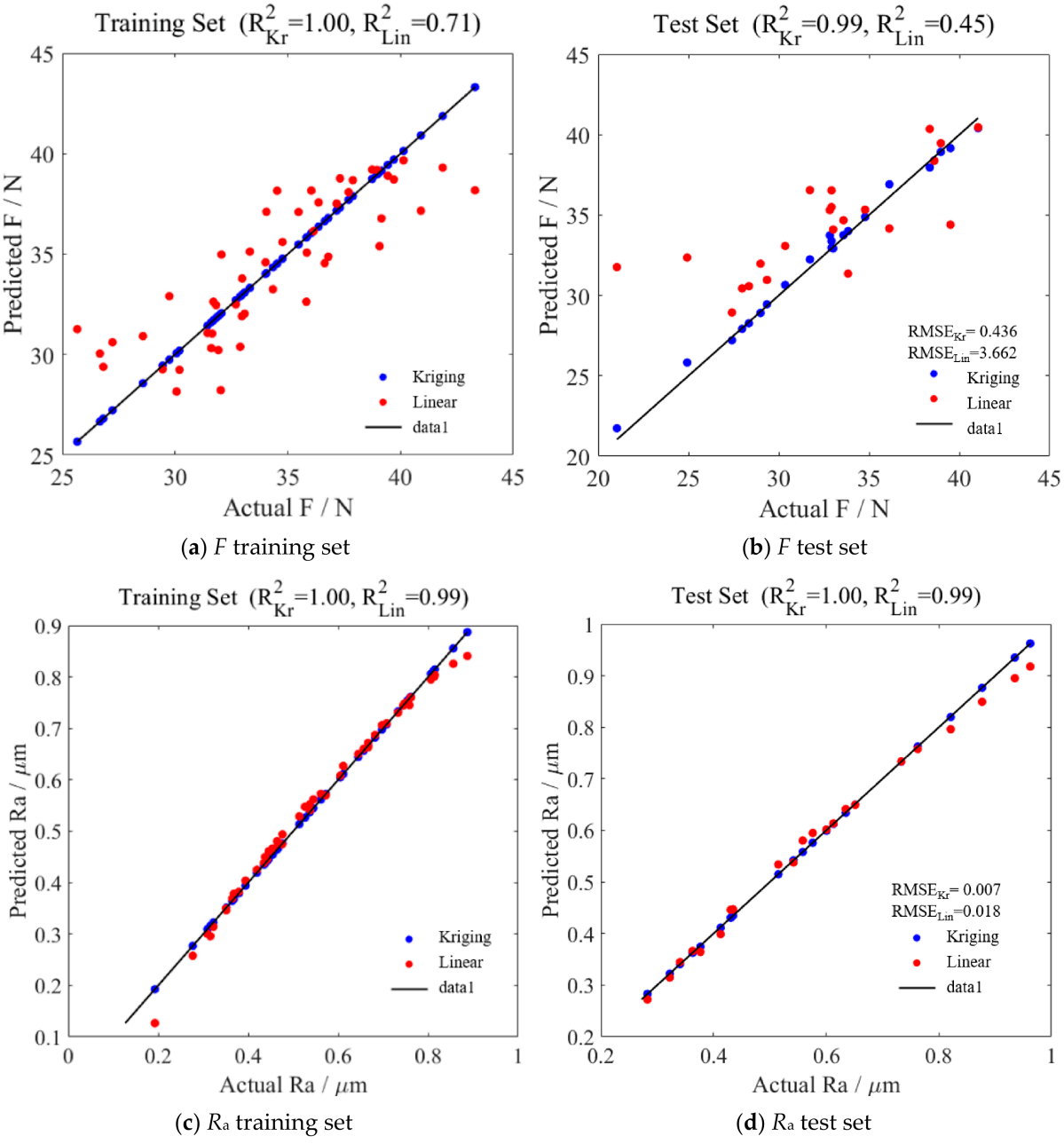
Run	a_e (mm)	n (rpm)	f_z (mm/z)	F (N)	R_a (μm)
1	0.43	10,100	0.015	33.012	0.4347
2	0.58	8550	0.011	31.700	0.542
3	0.23	7400	0.018	26.817	0.3940
4	0.54	6650	0.023	43.308	0.8558
...	...	...	...	...	...
71	0.46	6300	0.016	39.507	0.6005
72	0.31	7250	0.025	30.357	0.6347

Note: Only selected Latin hypercube sampling data are shown in the table; the ellipses indicate the omitted intermediate data for Runs 5–70.

The ranges of the machining parameters are defined as follows: 0.2 mm $\le a_e \le$ 0.6 mm, 0.01 mm/z $\le f_z \le$ 0.03 mm/z, and 6000 rpm $\le n \le$ 12,000 rpm.

The prediction performances of the Kriging and linear regression models for the milling force (F) and surface roughness (R_a) on the training and testing datasets are presented in Figure 12. For the prediction of F, the linear regression model achieves a coefficient

of determination R^2_{Lin} of 0.45 with an RMSE of 3.662 on the testing dataset, whereas the Kriging model achieves an R^2_{Kr} of 0.99 with an RMSE of 0.436. For the prediction of R_a, although the linear regression model already exhibits satisfactory predictive accuracy, the Kriging model further reduces the RMSE from 0.018 to 0.007. These results demonstrate that the developed Kriging models provide superior predictive performance and are therefore suitable for the subsequent multi-objective optimization analysis.



(**a**) F training set (**b**) F test set

(**c**) R_a training set (**d**) R_a test set

Figure 12. Comparison of the Kriging and linear regression models for predicting the milling force (F) and surface roughness (R_a).

The main parameters of the NSGA-II algorithm are set as follows: the maximum number of generations (MaxGen) is 100, the crossover probability ($p_{Crossover}$) is 0.5, and the population size (n_{pop}) is 40. After the iterative optimization converges, the Pareto front shown in Figure 13 is obtained, yielding 40 Pareto-optimal solutions.

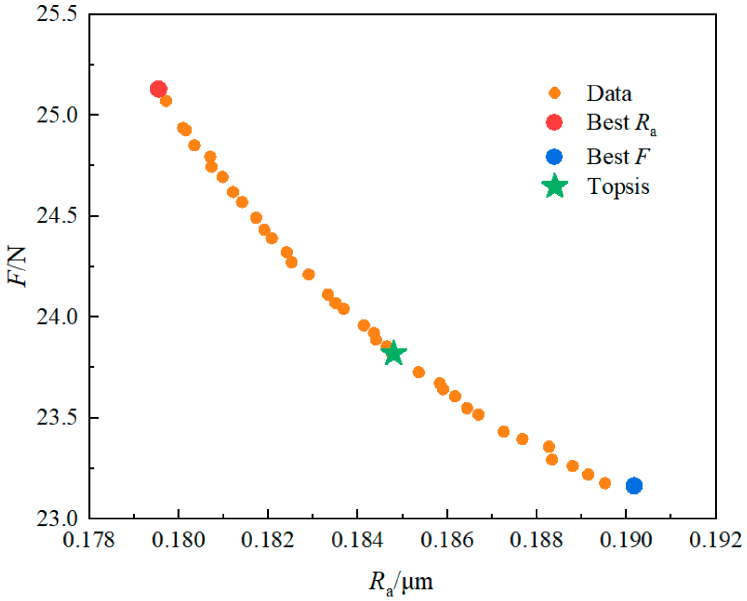


Figure 13. Pareto front for the multi-objective optimization of the milling force (F) and surface roughness (R_a).

The entropy-weight TOPSIS method is then applied to comprehensively evaluate the Pareto solution set. The optimal machining parameters are determined as a_e = 0.2101 mm, n = 10,090.7 rpm, and f_z = 0.01 mm/z. The validation experiment conducted under the optimized machining parameters was repeated three times. The predicted milling force and surface roughness are 23.82 N and 0.1848 μm, respectively, whereas the corresponding experimental values are 24.482 N and 0.193 μm. The relative errors between the predicted and experimental results are 2.70% for F and 4.25% for R_a, respectively. The prediction errors are small, demonstrating that the proposed optimization method provides high predictive accuracy.

5. Conclusions

To address the urgent demand for high-quality, low-damage machining of Mo and the limited research available in this field, single-factor and response surface milling experiments were conducted to clarify the relationships among the key milling parameters, response variables, and white layer characteristics and to optimize the milling process parameters. The main conclusions are summarized as follows:

- The single-factor milling experiments show that both the milling force (F) and surface roughness (R_a) increase with increasing feed per tooth (f_z) and radial depth of cut (a_e), whereas both decrease with increasing spindle speed (n).
- As the feed per tooth (f_z) increases, both the milling force and the white layer thickness increase. A higher milling force intensifies the compressive and plastic deformation imposed on the machined surface, thereby promoting grain refinement in the surface layer. The white layer remains predominantly composed of Mo, indicating that its formation is mainly associated with the microstructural evolution of the near-surface region of the Mo substrate.
- Response surface analysis reveals the relationships between the machining parameters (a_e, f_z, and n) and the response variables (F and R_a). Among the investigated parameters, spindle speed (n) has the greatest influence on the milling force, whereas feed per tooth (f_z) has the most significant effect on surface roughness.
- A Kriging surrogate model is established based on Latin hypercube sampling data and combined with the NSGA-II algorithm and the entropy-weight TOPSIS method for

multi-objective optimization. For the objective of simultaneously minimizing F and R_a, the optimal machining parameters within the investigated parameter ranges are determined as a_e = 0.2101 mm, n = 10,090.7 rpm, and f_z = 0.01 mm/z. Under the optimized conditions, the experimentally measured milling force and surface roughness are 24.482 N and 0.193 μm, respectively. The relative errors between the predicted and experimental results are 2.70% for F and 4.25% for R_a, respectively, demonstrating the high predictive accuracy and effectiveness of the proposed optimization approach.

Author Contributions: Conceptualization, X.M., J.C. and H.H.; methodology, X.M., J.C. and X.C.; software, H.X. and H.L.; validation, H.X., H.L. and X.C.; formal analysis, H.L.; investigation, H.X., J.G. and C.Y.; resources, J.C.; data curation, H.X. and H.L.; writing—original draft preparation, H.X.; writing—review and editing, X.M. and X.C.; visualization, H.X., J.G. and C.Y.; supervision, X.M., C.Y. and H.H.; project administration, X.M., J.G. and H.H.; funding acquisition, X.M. All authors have read and agreed to the published version of the manuscript.

Funding: This work was supported by the Strategic Priority Research Program of the Chinese Academy of Sciences (No. XDA 0380604) and the National Natural Science Foundation of China (No. 12535016).

Data Availability Statement: The original contributions presented in this study are included in the article. Further inquiries can be directed to the corresponding authors.

Conflicts of Interest: The authors declare no conflict of interest.

References

1. Xing, H.; Zhang, X.; Wang, H.; Chu, Q.; Zhang, W.; Li, Y.; Xu, L.; Hu, P.; Wang, Q.; Feng, R.; et al. Low-energy hydrogen ion irradiation effect on the surface defects of powder metallurgy molybdenum. *Int. J. Refract. Met. Hard Mater.* **2025**, *128*, 106980. [CrossRef]
2. Liu, Y.L.; Ding, F.; Luo, G.N.; Chen, C.A. Finite-temperature H behaviors in tungsten and molybdenum: First-principles total energy and vibration spectrum calculations. *Nucl. Fusion* **2017**, *57*, 126024. [CrossRef]
3. Sinclair, G.; Tripathi, J.K.; Diwakar, P.K.; Hassanein, A. Melt layer erosion during ELM-like heat loading on molybdenum as an alternative plasma-facing material. *Sci. Rep.* **2017**, *7*, 12273. [CrossRef] [PubMed]
4. Gökçe, H.; Çiftçi, İ.; Demir, H. Cutting parameter optimization in shoulder milling of commercially pure molybdenum. *J. Braz. Soc. Mech. Sci. Eng.* **2018**, *40*, 360. [CrossRef]
5. Zhang, J.; Du, J.; Li, B.; Su, G. Investigation on white layer formation in dry high-speed milling of nickel-based superalloy GH4169. *Machines* **2023**, *11*, 406. [CrossRef]
6. Li, L.; Lai, D.; Ji, Q.; Huang, J.; Lin, Y.; Pan, M.; Wei, J.; He, S. Influence of tool characteristics on white layer produced by cutting hardened steel and prediction of white layer thickness. *Int. J. Adv. Manuf. Technol.* **2021**, *113*, 1215–1228. [CrossRef]
7. Ekinovic, S.; Dolinsek, S.; Jawahir, I.S. Some observations of the chip formation process and the white layer formation in high speed milling of hardened steel. *Mach. Sci. Technol.* **2004**, *8*, 327–340. [CrossRef]
8. Umbrello, D.; Rotella, G. Experimental analysis of mechanisms related to white layer formation during hard turning of AISI 52100 bearing steel. *Mater. Sci. Technol.* **2012**, *28*, 205–212. [CrossRef]
9. Tong, X.; Zhang, H.; Qu, Q. Investigation on the influence of mesoscale geometric features on the surface white layer characteristics in titanium alloy milling using ball end mills. *Proc. Inst. Mech. Eng. Part B J. Eng. Manuf.* **2025**, *239*, 1934–1949. [CrossRef]
10. Mouralova, K.; Benes, L.; Prokes, T.; Zahradnicek, R.; Bednar, J.; Otoupalik, J.; Fiserova, Z.; Fiala, Z. Micro-milling machinability of pure molybdenum. *Int. J. Adv. Manuf. Technol.* **2019**, *102*, 4153–4165. [CrossRef]
11. Brown, M.; M'Saoubi, R.; Crawforth, P.; Mantle, A.; McGourlay, J.; Ghadbeigi, H. On deformation characterisation of machined surfaces and machining-induced white layers in a milled titanium alloy. *J. Mater. Process. Technol.* **2022**, *299*, 117378. [CrossRef]
12. Marçal, L.A.B.; Dierks, H.; Bushlya, V.; Lazar, I.; Dzhigaev, D.; Ren, Z.; Rysov, R.; Björling, A.; Sprung, M.; Mikkelsen, A.; et al. Spatially resolved structural and chemical properties of the white layer in machined Inconel 718 super alloy. *Mater. Des.* **2024**, *239*, 112789. [CrossRef]
13. Hassanpour, H.; Sadeghi, M.H.; Rasti, A.; Shajari, S. Investigation of surface roughness, microhardness and white layer thickness in hard milling of AISI 4340 using minimum quantity lubrication. *J. Clean. Prod.* **2016**, *120*, 124–134. [CrossRef]
14. Xu, J.; Yan, F.; Li, Y.; Yang, Z.; Li, L. Multiobjective Optimization of Milling Parameters for Ultrahigh-Strength Steel AF1410 Based on the NSGA-II Method. *Adv. Mater. Sci. Eng.* **2020**, *2020*, 8796738. [CrossRef]

15. Qu, S.; Zhao, J.; Wang, T. Experimental study and machining parameter optimization in milling thin-walled plates based on NSGA-II. *Int. J. Adv. Manuf. Technol.* **2017**, *89*, 2399–2409. [CrossRef]
16. Lu, X.; Zhang, Y.; Sun, Z.; Gu, H.; Jiang, C.; Liang, S.Y. Multi-objective optimization of cutting parameters for micro-milling nickel-based superalloy thin-walled parts based on improved NSGA-II algorithm. *Int. J. Adv. Manuf. Technol.* **2024**, *135*, 775–786. [CrossRef]
17. Zhou, G.; Zhang, C.; Lu, F.; Zhang, J. Integrated optimization of cutting parameters and tool path for cavity milling considering carbon emissions. *J. Clean. Prod.* **2020**, *250*, 119454. [CrossRef]
18. Li, C.; Zhao, G.; Meng, F.; Yu, S.; Yao, B.; Liu, H. Multi-objective optimization of machining parameters in complete peripheral milling process with variable curvature workpieces. *J. Manuf. Process.* **2024**, *117*, 95–110. [CrossRef]
19. Wu, S.; Liu, G.; Zhang, W.; Chen, W.; Wang, C. Formation mechanism of white layer in the high-speed cutting of hardened steel under cryogenic liquid nitrogen cooling. *J. Mater. Process. Technol.* **2022**, *302*, 117469. [CrossRef]
20. Lee, E.H.; Shaffer, B.W. The theory of plasticity applied to a problem of machining. *J. Appl. Mech.* **1951**, *18*, 405–413. [CrossRef]
21. Ozlu, E.; Molinari, A.; Budak, E. Two-zone analytical contact model applied to orthogonal cutting. *Mach. Sci. Technol.* **2010**, *14*, 323–343. [CrossRef]
22. Lai, F.; Hu, A.; Mao, K.; Wu, Z.; Lin, Y. Effect of milling processing parameters on the surface roughness and tool cutting forces of T2 pure copper. *Micromachines* **2023**, *14*, 224. [CrossRef] [PubMed]
23. Kelly, A.; Leonhardt, T.A.; Sauer, J.P. Metallography and microstructures of refractory metals and alloys. In *ASM Handbook*; Vander Voort, G.F., Ed.; Metallography and microstructures; ASM International: Materials Park, OH, USA, 2004; Volume 9, pp. 877–888.
24. Li, D.; Yu, J.; Zheng, X.; Yue, C.; Ding, L.; Liu, Y. Exploration of tunable, low-depletion novel resistor paste system based on molybdenum-based functional phase modulation. *J. Mater. Sci. Mater. Electron.* **2023**, *34*, 1957. [CrossRef]
25. Qi, Y.; Zhang, J.; Yi, M.; Xu, C.; Zhang, P.; Chen, Z.; Li, G. Study on the grain refinement mechanism of the machined surface of Inconel 718. *J. Mater. Res. Technol.* **2024**, *29*, 1729–1743. [CrossRef]

Disclaimer/Publisher's Note: The statements, opinions and data contained in all publications are solely those of the individual author(s) and contributor(s) and not of MDPI and/or the editor(s). MDPI and/or the editor(s) disclaim responsibility for any injury to people or property resulting from any ideas, methods, instructions or products referred to in the content.